JOURNAL OF GEOPHYSICAL RESEARCH, VOL. 98, NO. C9, PAGES 16,411–16,425, SEPTEMBER 15, 1993

Airborne Synthetic Aperture Radar Observations and Simulations for Waves in Ice

PARIS W. VACHON,[1] RICHARD B. OLSEN,[2] HARALD E. KROGSTAD,[3] AND ANTONY K. LIU[4]

The Canada Centre for Remote Sensing CV-580 aircraft collected C-band synthetic aperture radar (SAR) data over the marginal ice zone off the east coast of Newfoundland during the Labrador Ice Margin Experiment (LIMEX) in March 1989. One component of the LIMEX'89 program was the study of ocean waves penetrating the marginal ice zone. In this paper, we consider nearly coincidental observations of waves in ice by airborne SAR and wave-induced ice motion measurements. We explain the wave patterns observed in the SAR imagery, and the corresponding SAR image spectra, in terms of SAR wave imaging models. These include the well-known tilt cross-section modulation, linear, quasi-linear, and nonlinear velocity bunching forward mapping models (FMMs), and the assertion that the concept of coherence time limitation applies differently to the cases of waves in ice and open water. We modify the concept of the scene coherence time to include two parts: first, a decorrelation time deduced from the inherent azimuth cutoff in the nonlinear velocity bunching FMM; and second, the intrinsic scene coherence time which is a measure of the time scale over which an open water Bragg scattering patch retains its phase structure. Either of these coherence time scales could dominate the SAR image formation process, depending upon the environmental conditions (the wave spectrum and the wind speed, for example). These two coherence time scales are independently estimated based upon a quasi-linear velocity bunching FMM applied to some of the LIMEX'89 observations. Observed SAR image spectra and forward mapped ice motion package spectra are favorably compared.

1. INTRODUCTION

The Labrador Ice Margin Experiment (LIMEX) '89 occurred in March and early April of 1989 over the marginal ice zone (MIZ) off the east coast of Newfoundland, Canada. LIMEX'89 is a multidisciplinary, multiinvestigator program involving many diverse research objectives [see *Tang and Manore*, 1992]. In this paper, we consider only the portion of LIMEX'89 which was concerned with observations of ocean surface waves penetrating the MIZ. The synthetic aperture radar (SAR) observations were acquired by the Canada Centre for Remote Sensing (CCRS) airborne C-band SAR [*Livingstone et al.*, 1988]. The surface observations were acquired by instrumentation deployed on ice floes by the field program which operated from M/V *Terra Nordica*.

SAR observations of waves in ice are being used to address two main research objectives: first, to provide a synoptic-scale overview for the study of wave evolution (e.g., wave attenuation, dispersion, and refraction) in the MIZ [*Liu et al.*, 1991*a*, *b*, 1992; *Raney et al.*, 1989; *Vachon and Bhogal*, 1990]; and second, to work toward an understanding of the SAR imaging physics for ocean waves by studying the simplified case (for SAR) of waves in ice. Here, we concentrate upon the latter objective, analyzing C-band SAR data of waves in ice acquired under a variety of aircraft geometries with respect to the observed wave field. A more complete summary of the LIMEX'89 SAR data sets is given by *Vachon and Bhogal* [1990].

For waves in ice the ice cover acts as a natural low-pass filter [*Raney*, 1981], essentially eliminating the high-frequency waves. This has two effects for the SAR: first, the SAR no longer relies upon Bragg scattering from time-dependent patches on the ocean surface; and second, the effective scene coherence time is lengthened. The ice cover also inhibits hydrodynamic modulation of radar cross section in terms of wave-wave interactions modifying the Bragg-scale waves. However, hydrodynamic-type modulation mechanisms do exist for waves in ice, such as differential tilting of ice floes to periodically expose floe edges or modulate the interstitial ice roughness. Such mechanisms are assumed to be of secondary importance relative to tilt modulation [*Vachon et al.*, 1988] for range traveling ocean waves. Thus the case of waves in ice allows direct observation of the velocity bunching SAR imaging mechanism and provides a solid basis for the study of directional spectra derived from SAR wave data.

In this paper, velocity bunching forward mapping models (FMMs) are applied to transform observed directional wave spectra into SAR image spectra. Three FMMs are used: first, a linear FMM [*Monaldo and Lyzenga*, 1986], modified for the case of airborne SAR; second, a quasi-linear FMM in which the linear model is augmented with a scene-dependent azimuth cutoff for coherence time limited SAR imaging; and third, a fully nonlinear FMM based upon an integral transformation of the wave spectrum [*Hasselmann and Hasselmann*, 1991; *Krogstad*, 1992]. The model validation is based upon directional wave spectra from wave-induced ice floe motion measurements collected by ice motion packages (IMPs) deployed on ice floes. The measured directional spectra may be mapped into SAR image spectra using the various FMMs and quantitatively compared with the observed SAR image spectra.

We demonstrate that there is good agreement between the forward mapped IMP spectra and the observed SAR image spectra, provided interlook motion is accounted for in processing the SAR image spectra [*Vachon and West*, 1992; *Vachon and Raney*, 1992]. However, extreme differences

[1]Canada Centre for Remote Sensing, Ottawa, Ontario, Canada.
[2]Satlantic Incorporated, Halifax, Nova Scotia, Canada.
[3]Foundation for Scientific and Industrial Research at the Norwegian Institute of Technology, Trondheim, Norway.
[4]NASA Goddard Space Flight Center, Greenbelt, Maryland.

Paper number 93JC00914.
0148-0227/93/93JC-00914$05.00

between spectra calculated in ice covered and nearby open water regions cannot be explained by the velocity bunching FMMs since the effective coherence time for the open water case is affected by more than just velocity bunching mapping. The differences may be explained by considering the intrinsic coherence of the Bragg scattering patches in open water. The effective lifetime of the Bragg scattering patches is affected by direct wind forcing and wave-wave interactions, which are not explicitly accounted for in any of the velocity bunching FMMs.

In section 2 we review SAR imaging theory for ocean waves with emphasis on the case of waves in ice. In section 3 we provide an overview of the relevant LIMEX'89 field program activities, concentrating upon coincident SAR and IMP measurements from March 26, 1989. In section 4 we first estimate the decorrelation time scale by tuning a quasi-linear FMM to match a nonlinear FMM. Then, we estimate the intrinsic scene coherence time scale by comparing SAR image spectra derived from nearby ice-covered and open water regions using a quasi-linear FMM. Finally, we compare observed SAR image spectra with simulated SAR image spectra based upon IMP directional wave spectra and the velocity bunching FMMs for waves in ice. The conclusions of the study are presented in section 5.

2. SAR Imaging Theory for Waves in Ice

The microwave scattering mechanism from the ocean surface for nonnadir and nongrazing angle SAR geometries is assumed to be Bragg scattering, in which a patch of short-scale roughness elements are selected by the local incidence angle and the radar wavelength [*Wright*, 1966]. If the group of Bragg-scale roughness elements retains phase lock while being illuminated by the radar, the Bragg scattering patch presents a coherent, point target-like signal to the SAR. The ocean surface is assumed to constitute a distribution of a large number of such Bragg scattering patches.

There are three principal mechanisms by which ocean waves modulate the spatial distribution of Bragg-scale roughness elements, thus allowing the ocean waves to be imaged by SAR. These mechanisms are tilt modulation, hydrodynamic straining, and velocity bunching [*Alpers et al.*, 1981; *Hasselmann et al.*, 1985; *Hasselmann and Hasselmann*, 1991]. Tilt modulation and hydrodynamic straining are assumed to be linear processes. For steep incidence angles, tilt modulation is often assumed to dominate the effects of hydrodynamic straining [*Monaldo and Lyzenga*, 1986]. However, the dominant source of wave contrast in SAR imagery is velocity bunching [*Alpers and Rufenach*, 1979; *Swift and Wilson*, 1979]. This typically nonlinear mechanism is a geometry-dependent mapping from the distribution of radar cross section in the scene into the SAR image domain and arises from coherent sensing of scatterer motion on the ocean surface due to the wave orbital velocity. The nonlinear nature of velocity bunching mapping has been described by many authors [see *Alpers and Rufenach*, 1979; *Raney*, 1981].

The mechanisms which act to enhance the wave contrast in a SAR image are suppressed by the ocean surface's partial coherence. The ocean surface is dynamic and changing while being illuminated by the radar. In order to achieve the full resolution potentially available in SAR imaging, the scene should remain static (coherent) while being imaged. The integration time is typically several seconds for an airborne C-band SAR; the ocean surface at short scales does not remain static for the required time scales [see *Kawai*, 1979]. The effect of this coherence time limitation is a reduction in achievable resolution in the SAR azimuth dimension [*Raney*, 1980] and consequently a degradation in the imaged ocean wave contrast.

The coherence time τ is modeled to consist of two separable parts: the decorrelation time τ_d is caused by the relative orbital motion of Bragg scattering patches within each SAR resolution cell [*Hasselmann et al.*, 1985; *Tucker*, 1985]; while the intrinsic scene coherence time τ_i is caused by changes in the population of Bragg scattering patches themselves due to wind forcing or wave-wave interaction. For purposes of SAR resolution calculation, these times are lumped together into an effective coherence time:

$$\frac{1}{\tau^2}=\frac{1}{\tau_d^2}+\frac{1}{\tau_i^2}. \tag{1}$$

In this combination, τ is dominated by the smaller of τ_d or τ_i.

The decorrelation time τ_d has previously been modeled as an integration over the ocean wave spectrum [*Tucker*, 1985], requiring selection of cutoff ocean wave length or frequency scales [*Hasselmann et al.*, 1985]. On the other hand, the intrinsic coherence time τ_i has never been explicitly quantified but for open ocean waves may be assumed to be a function of the surface roughness (wind stress and wave age) and hydrodynamic modulation of the Bragg-scale waves.

In this work we apply a velocity bunching FMM to observed directional wave spectra in order to simulate SAR image spectra. The use of waves-in-ice data is a valuable case for coherence time studies since the ice cover is essentially a solid surface. Therefore it may be assumed that τ_i for waves in ice is large relative to τ_i for open water waves. Furthermore, it may be assumed that τ_i for waves in ice is large relative to the SAR integration time. Therefore, when using a velocity bunching FMM for the case of waves in ice, the effects of τ_i may be completely neglected. There are at least three ways of accounting for τ_d in a velocity bunching FMM: first, we can simply ignore the coherence time effect completely and use a linear FMM; second, we can tune a quasi-linear FMM, which consists of the linear FMM and an azimuth wavenumber cutoff function, to fit the fully nonlinear FMM; and third, we can use the fully nonlinear velocity bunching FMM [*Hasselmann and Hasselmann*, 1991; *Krogstad*, 1992], which contains the effects of τ_d implicitly as an inherent azimuth cutoff [*Krogstad*, 1992]. Regardless of the way in which τ_d is included, we assume for waves in ice that the initial distribution of radar cross section is due only to tilt cross-section modulation and that the SAR image is dominated by velocity bunching.

2.1. *Ocean Wave Model*

Assume that we are observing an ocean wave system on a flat Earth with a generic airborne SAR. We describe the ocean waves by linear superposition of discrete sinusoidal ocean wave components. Then, in the (x, y, z) coordinate system (see Figure 1) for which x is along the SAR track, y is along the SAR ground range, and z is vertical, we describe the ocean wave height by the following summation of sinusoidal wave components [*Borgman*, 1979]:

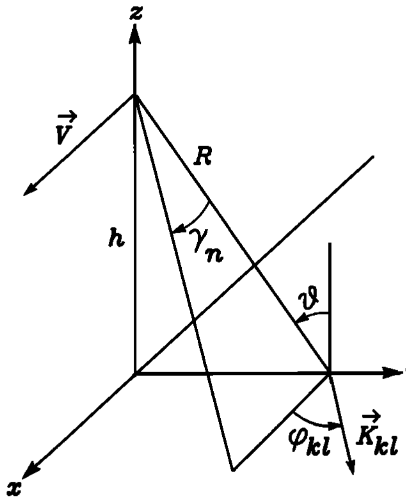

Fig. 1. Diagram of airborne SAR geometry: x is the azimuth dimension; y is the ground range dimension; z is the height dimension; $\vec{V}$ is the platform velocity; h is the platform altitude; R is the scene range; ϑ is the scene incidence angle; γ_n is the angular offset to the nth look; $\vec{K}_{kl}$ is the wavenumber for spectral component (k, l); and φ_{kl} is its aspect angle.

$$\eta(x, y, t) = \sum_k \sum_l A_{kl} \cos (K_k x + K_l y - \Omega_{kl} t + \psi_{kl}), \tag{2}$$

where k and l are counting indices for the azimuth and ground range directions, respectively, A_{kl} is the wave component amplitude, $K_{kl} = (K_k^2 + K_l^2)^{1/2}$ is the ocean wavenumber, $\Omega_{kl} = (gK_{kl})^{1/2}$ (assuming the linear deepwater dispersion relation), and ψ_{kl} is a random phase term which is uniformly distributed on $0 \leq \psi_{kl} < 2\pi$. We define the wave component phase as

$$\arg_{kl}(x, y, t) = K_k x + K_l y - \Omega_{kl} t + \psi_{kl}. \tag{3}$$

The wave amplitude components may be related to the one-sided (directionally unambiguous) directional wavenumber spectral density Ψ of η by

$$A_{kl} = [\Psi(K_k, K_l) dK_x dK_y]^{1/2}, \tag{4}$$

where dK_x and dK_y are wavenumber increments on the azimuth and ground range wavenumber axes for the intervals occupied by the (k, l) wave component. Then, the significant wave height is

$$H_s = 4[\int\int \Psi(K_k, K_l)\, dK_x\, dK_y]^{1/2}, \tag{5}$$

and mean wavelength is

$$\Lambda_0 = 2\pi \frac{\int\int \Psi(K_k, K_l)\, dK_x\, dK_y}{\int\int K_{kl}\Psi(K_k, K_l)\, dK_x\, dK_y}. \tag{6}$$

Figure 1 shows the generalized geometry for a SAR/ocean wave system. In the diagram, $\vec{V}$ is the platform velocity vector which lies along the x axis, h is the platform altitude, R is the slant range to the location of interest in the scene, ϑ is the local incidence angle, and $\varphi_{kl} = \tan^{-1}(K_l, K_k)$ is the wave aspect angle. In Figure 1, γ_n represents the angular offset (in the SAR processor) to the nth look, which leads to a spatial offset of the nth look of $\Delta x_n \sim R\gamma_n$.

The SAR is assumed to be moving along the x axis with uniform speed V. The nth look is then observed at time

$$t = \frac{x - \Delta x_n}{V}, \tag{7}$$

where the initial x coordinate has been assumed to be zero. Substituting for t in (2), we find that the phase term for the nth look becomes

$$\arg_{kl}^n (x, y) = \left(K_k - \frac{\Omega_{kl}}{V}\right)x + K_l y + \Omega_{kl} \frac{\Delta x_n}{V} + \psi_{kl}. \tag{8}$$

The encountered azimuth wavenumber is

$$\tilde{K}_k = K_k - \frac{\Omega_{kl}}{V}, \tag{9}$$

which may cause considerable spectral distortion for an aircraft SAR system in which the wave phase speed is an appreciable fraction (say 10–15%) of the platform velocity. In that case, the distortion may be corrected by a spectral interpolation procedure using the wave dispersion relation [*Vachon et al.*, 1988].

On the basis of the third phase term of (8) the SAR image of the nth look is shifted in phase by the amount

$$\Omega_{kl} \frac{\Delta x_n}{V} = -\Omega_{kl} t_n, \tag{10}$$

where t_n is the temporal offset to nth look. This spatial offset has implications for the unique resolution of the ocean wave propagation direction [*Vachon and Raney*, 1991] and has lead to the "spectral-phase-shift" (SPS) method [*Vachon and West*, 1992] of processing SAR image spectra. This method accounts for lost contrast in the image due to relative motion between the wave images in the individual looks [*Vachon and West*, 1992; *Vachon and Raney*, 1992] and has been used to calculate some of the SAR image spectra considered in this paper.

The ocean wave height which is observed for the nth look may be written in the simplified form

$$\eta^n(x, y) = \sum_k \sum_l A_{kl} \cos [\arg_{kl}^n (x, y)], \tag{11}$$

which can be related to other linear wave properties for a particular look using linear transfer functions.

2.2. *Modulation Transfer Function*

The modulation transfer function (MTF) is often a convenient representation for the relationship between an observed SAR image spectrum and the actual ocean wave spectrum [*Alpers et al.*, 1981]. Let $S^n(K_k, K_l)$ represent the raw SAR image spectrum for the nth look. This spectrum has been corrected for the system transfer function [*Beal et al.*, 1983], speckle noise bias [*Goldfinger*, 1982], and scanning distortion [*Vachon et al.*, 1988] and has been normalized by the mean radar cross section squared. If the MTF is linear, it is only a function of the ocean wavenumber and the SAR geometry. Then, the SAR image spectrum is related to the ocean wave spectrum via

$$S^n(K_k, K_l) = R^2(K_k, K_l)\Psi(K_k, K_l), \quad (12)$$

where $R^2(K_k, K_l)$ is the MTF. An alternate form for the MTF is in terms of the slope spectrum, in which case the MTF is divided by K_{kl}^2. This linear MTF approach is useful for representing the effects of local tilting and, under some circumstances, velocity bunching. In this paper, we consider a quasi-linear MTF in which R^2 is modified by a scene-dependent azimuth cutoff function whose width is given by the effective scene coherence time τ.

2.3. *Tilt MTF for Waves in Ice*

For the moment, assume that the spatial distribution of wave image contrast observed by a SAR is due to the tilt cross-section modulation mechanism. This mechanism is linear in nature and is related to the local surface slope in the range direction due to the ocean wave system. For a particular wave component the observed distribution of radar cross section due to tilt modulation is given by

$$\sigma_t^o(x, y) = \sigma^o \left\{ 1 + \sum_k \sum_l \frac{1}{\sigma^o} \frac{\partial \sigma^o}{\partial \theta} \Bigg|_{\theta_0} \cdot K_l A_{kl} \sin\left[\arg_{kl}^n (x, y)\right] \right\}, \quad (13)$$

where σ^o is the local mean radar cross section, θ_0 is the local incidence angle, and $\partial\sigma^0/\partial\theta$ represents the modulation in the image due to changes in local surface slope in the plane of radar illumination.

The tilt modulation transfer function (MTF) was formulated for ocean waves by *Alpers et al.* [1981] as

$$\vec{R}_t = -iK_l \frac{1}{\sigma^o} \frac{\partial \sigma^o}{\partial \theta} \Bigg|_{\theta_0}, \quad (14)$$

which in general is a function of wind stress and wind direction for open ocean waves and a function of ice type for waves in ice. *Monaldo and Lyzenga* [1986] provided a simple tilt MTF model based upon Bragg scattering and a fully developed Phillips spectrum:

$$\vec{R}_t = iK_l \frac{4 \cot \theta}{1 \pm \sin^2 \theta}, \quad (15)$$

where positive holds for vertical polarization and negative holds for horizontal polarization. This model is independent of wind speed and radar wavelength. $|R_t|/K_l$ is plotted in Figure 2. This model predicts that tilt modulation is largest for HH polarization.

The derivation of the tilt MTF for waves in ice was first done for LIMEX'87 data in [*Vachon et al.*, 1988] using data from the CCRS SAR. In that case, the relatively small magnitude of the tilt MTF was used to rule it out as the dominant imaging mechanism for waves-in-ice. The relative radar cross section was derived for a uniform image of ice for C-band SAR image data with VV polarization.

Using a least squares fit, a second-order polynomial in local incidence angle θ may be fitted to the logarithmic relative radar cross-section data giving

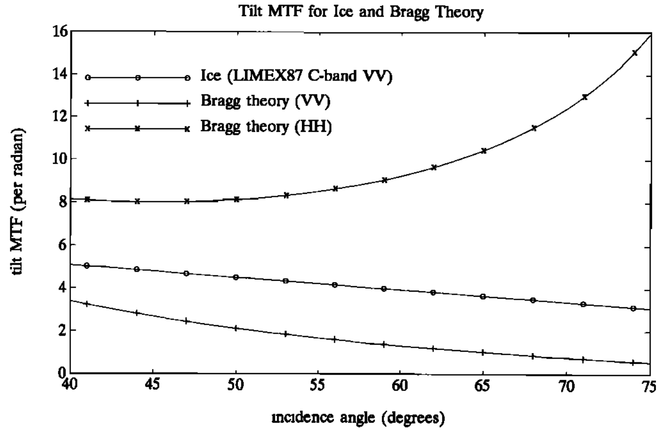

Fig. 2. Tilt MTF $|\vec{R}_t|/K_l$ as a function of incidence angle for uniform ice derived from LIMEX'87 VV SAR image data and for an open water Bragg scattering model for HH and VV polarization.

$$10 \log_{10} (\sigma^o) = A\theta^2 + B\theta + C. \quad (16)$$

Then, the tilt MTF is found to be

$$\vec{R}_t = iK_l \frac{180}{\pi} \frac{\log(10)}{10} (2A\theta + B). \quad (17)$$

For the LIMEX'87 data we found that $A = 0.0022 \pm 0.0004$ and $B = -0.56 \pm 0.05$ for θ expressed in degrees. $|\vec{R}_t|/K_l$ for waves in ice is plotted in Figure 2 and is seen to be of the same order of magnitude as the open ocean tilt MTF. Note that this empirical technique of deriving the tilt MTF does not require absolute calibration of the SAR image but does require relative calibration. The tilt MTF calculation has been completed using LIMEX'89 airborne SAR imagery with results of similar magnitude. In any case, tilt modulation alone leads to a rather small wave contrast and is of rather minor importance in the context of velocity bunching.

2.4. *Velocity Bunching*

2.4.1. *Linear FMM.* The pattern of ocean surface reflectivity, arising from tilt modulation and any other local cause, is modified and redistributed in the SAR image azimuth dimension through the velocity bunching imaging mechanism [*Alpers and Rufenach*, 1979; *Swift and Wilson*, 1979]. The SAR senses the radial component of the wave orbital velocity imparted upon a scattering patch at each spatial location in the scene and maps the corresponding signal to the image in a location that is shifted in the azimuth dimension in proportion to the radial velocity. This imaging problem reduces to a straightforward spatial mapping.

For a particular wavenumber component the projected orbital velocity along the radial line of sight toward the SAR in the nth look is

$$u_r^n(x, y) = \sum_k \sum_l A_{kl}\Omega_{kl} \cos \vartheta\, l(\vartheta, \varphi_{kl}) \cdot \sin\left[\arg_{kl}^n (x, y) + \tan^{-1} (\sin \varphi_{kl} \tan \vartheta, -1)\right], \quad (18)$$

where $l(\vartheta, \varphi_{kl}) = (1 + \sin^2 \varphi_{kl} \tan^2 \vartheta)^{1/2}$. The azimuth image variable is then subject to the mapping function [*Raney*, 1971]

$$x = x' + \frac{R}{V} u_r^n(x', y) = x' + \xi(x', y), \tag{19}$$

where x is the image azimuth variable, x' is the scene azimuth variable, and $\xi(x', y)$ is the field of azimuth image shifts.

If x is monotonically increasing, then the redistribution of radar cross section due to velocity bunching is

$$\sigma_{t,vb}^o(x, y) = \sigma_t^o[x \rightarrow x' + \xi(x', y), y] \, |\partial x/\partial x'|^{-1}, \tag{20}$$

and if the magnitude of the azimuth shift field is small, this mapping function gives the linear MTF for velocity bunching:

$$\vec{R}_{vb} = g^{1/2} \frac{h}{V} K_{kl}^{3/2}\left(1 - \frac{\Omega_{kl}}{VK_k}\right) \cos \phi_{kl} l(\theta, \phi_{kl}) \cdot \exp \{i \tan^{-1} (\sin \phi_{kl} \tan \theta, -1)\}. \tag{21}$$

This is similar to a well-known result [see *Monaldo and Lyzenga*, 1986], modified here to include the along-track scanning distortion for airborne SAR.

A complete linear MTF includes tilt and velocity bunching modulation as the coherent sum of the two individual contributions:

$$\vec{R} = \vec{R}_t + \vec{R}_{vb}. \tag{22}$$

Other linear transfer functions may be included in this formulation. Then

$$S^n(K_k, K_l) = |\vec{R}_t + \vec{R}_{vb}|^2 \Psi(K_k, K_l), \tag{23}$$

which is also a well-known result. In this FMM, each look and the look-summed image have identical spectra. However, the time step between successive looks tends to degrade the spectral contrast at a given wavenumber. Therefore the relation of (23) best matches the SAR image spectrum of an individual look, or a look-summed spectrum which has had the relative motion between looks correctly compensated.

2.4.2. *Quasi-linear FMM.* Scene coherence time effects may be included in the linear model in an ad hoc manner by including the effect of azimuth resolution degradation caused by a finite scene coherence time. The generalized SAR azimuth resolution may be written [*Vachon*, 1987]

$$\rho = \rho_1[N^2 + (T/\tau)^2]^{1/2}, \tag{24}$$

where $\rho_1 = V/B$ is the single look SAR azimuth resolution, N is the number of looks processed, T is the SAR coherent integration time, and B is the available Doppler bandwidth. For the case of coherence time-limited imaging ($N\tau \ll T$), the second term dominates. Assuming a Gaussian-shaped impulse response, an azimuth cutoff function is then imposed in the wavenumber domain. The following augmentation to the linear FMM then applies:

$$S(K_k, K_l) = H_d(\bar{K}_k) \, |\vec{R}_t + \vec{R}_{vb}|^2 \Psi(K_k, K_l), \tag{25}$$

where $H_d(\bar{K}_k)$ is an azimuth-oriented, low-pass filter function with cutoff wavenumber governed by the coherence time τ. This model is termed quasi-linear since τ may be mildly dependent upon the wave spectrum itself. The azimuth filter function may be approximated as a Gaussian function [*Raney*, 1980]:

$$H_d(\bar{K}_k) = \exp \{-\pi(\bar{K}_k/K_c)^2\}, \tag{26}$$

where K_c is the equivalent rectangular cutoff wavenumber, which may be related to the cutoff wave length scale (waves of shorter scale will not be imaged by the SAR) by $\Lambda_c = 2(2\pi/K_c)$. The corresponding coherence time is then

$$\tau = \frac{\lambda}{2(2)^{1/2}} \left(\frac{R}{V}\right) K_c. \tag{27}$$

There may be several different contributions to the effective scene coherence time, as noted previously.

2.4.3. *Nonlinear FMM.* The general velocity bunching FMM is more complicated if (19) is not monotonically increasing or if its derivative is not small. In this case, velocity bunching is nonlinear. If (19) is differentiable for all x, then, following *Parzen* [1962], there are $m(x)$ points $x_1(x), x_2(x), \cdots, x_m(x)$ such that for $k = 1, 2, \cdots, m(x)$,

$$x_k = x' + \xi(x', y), \tag{28}$$

and

$$\partial x/\partial x'|_{x_k} \neq 0. \tag{29}$$

Then

$$\sigma_{t,vb}^o(x, y) = \sum_{k=1}^{m(x)} \sigma_t^o(x_k, y) \left| \frac{\partial x}{\partial x'} \right|^{-1} \quad \text{if } m(x) > 0 \tag{30}$$

$$\sigma_{t,vb}^o(x, y) = 0 \quad \text{if } m(x) = 0 \tag{31}$$

The contribution to the SAR image reflectivity map is composed of the summation over contributions from all inflections of the mapping function. Equation (30) represents the general case of velocity bunching mapping. It includes the linear transfer function of (23), the effects of scene decorrelation [*Krogstad*, 1992] and the fully nonlinear nature of velocity bunching. Note that there is one such mapping for each individual look. The mapping applies correctly to the look-summed image if the phase shift due to scene motion between successive looks is small.

The SAR image may be predicted using (30) for each set of input ocean wave conditions. One way of obtaining the corresponding SAR image spectrum is via a Monte Carlo simulation [*Alpers*, 1983] in which a representative SAR image is calculated by explicitly calculating the mapping over an ensemble of point scatterers. The SAR image spectrum then follows by calculating the Fourier transform of the resulting image and performing ensemble averaging.

More direct calculations have recently appeared in the literature in which the Fourier transform of (30) is explicitly calculated under the assumption of Gaussian linear wave theory [*Hasselmann and Hasselmann*, 1991; *Krogstad*, 1992]. It can be shown that for the nth look, the SAR image spectrum is given by the integral transformation

$$S^n(K_k, K_l) = \int_x \int_y \exp \{i(K_k x + K_l y)\} G(x, y; K_k) \, dx dy, \tag{32}$$

where

$$G(x, y; K_k) = \sigma_t^{o2} \exp\{-K_k^2(\rho_{\xi\xi}(0, 0) - \rho_{\xi\xi}(x, y))\}$$
$$\cdot\{1 + \rho_{\sigma\sigma}(x, y) + iK_k[\rho_{\sigma\xi}(x, y)$$
$$- \rho_{\sigma\xi}(-x, -y)]$$
$$+ K_k^2[(\rho_{\sigma\xi}(0, 0) - \rho_{\sigma\xi}(x, y))(\rho_{\sigma\xi}(0, 0)$$
$$- \rho_{\sigma\xi}(-x, -y))]\}, \tag{33}$$

and each function ρ is a covariance function for σ_t^o and ξ. These covariance functions are calculated from the scanning distorted wave spectrum and the corresponding linear transfer functions. In practice, this nonlinear FMM is calculated as a finite series expansion in K_k of (33) [*Krogstad*, 1992], with a suitable number of terms retained, depending upon the degree of velocity bunching nonlinearity. Suitable accounting for motion between looks must be made in order to properly compare actual SAR image spectra with forward mapping results predicted by (32).

The azimuth cutoff arising from the nonlinear FMM is a measure of the decorrelation coherence time scale. The azimuth cutoff is scaled by the standard deviation of the azimuth shift:

$$\sigma_\xi = [\rho_{\xi\xi}(0)]^{1/2}. \tag{34}$$

This shift is proportional to R/V and is a function of the geometry and of the properties of the wave spectrum itself. In the asymptotic analysis of *Krogstad* [1992] the nondimensional azimuth wavenumber was defined as

$$\kappa = K_k\sigma_\xi. \tag{35}$$

Then, the inherent azimuth cutoff in the nonlinear velocity bunching FMM occurs near $\kappa = 2$, below which the quasi-linear FMM should be a reasonable approximation to the nonlinear FMM. The linear FMM should be a reasonable approximation to the nonlinear FMM when $\kappa \ll 1$. Using (4), (5), (6), and (18), it can be shown that for steep (near-nadir) incidence angles,

$$\sigma_\xi \sim \left(\frac{R}{V}\right)\left(1 - \frac{\sin^2(\vartheta)}{2}\right)^{1/2}\left(\frac{\pi g}{8\Lambda_0}\right)^{1/2} H_s. \tag{36}$$

This expression provides a useful indication of the azimuth cutoff as a function of readily observable wave properties.

3. LIMEX'89 OBSERVATIONS

We now consider the measurements taken during LIMEX'89 that directly relate to this SAR/wave study. Simultaneous observations of ocean waves propagating into the MIZ were taken by the CCRS CV-580 airborne SAR and by IMPs placed upon ice floes from M/V *Terra Nordica*. The objective was to process the IMP data into directional spectra for waves in ice and to subject those spectra to the various velocity bunching FMMs for direct comparison with the observed SAR image spectra.

On March 26, 1992, a study site was selected near 50°N 52.5°W. This was an area of uniform ice type in which the ice floes were substantial enough to support instrumentation and personnel. We concentrate on the data from March 26 since a pronounced bimodal wave system was present.

3.1. *Observed Conditions*

Meteorological conditions during LIMEX were dominated by a series of low-pressure systems passing over the region, propagating from the west and southwest into the Labrador Sea and North Atlantic. The dominant wind direction was such that the ice pack drifted eastward and dispersed, extending 300 to 500 km offshore.

On March 25, 1989, a low-pressure system passed to the south of Greenland and generated large waves which propagated through the ice pack and into the study site. These waves arrived at the M/V *Terra Nordica* location with a 280-m wavelength, propagated toward the west and southwest, and had a significant wave height of about 0.8 m. The swell persisted from March 25 to 30.

On March 26, a low-pressure system developed south of Nova Scotia, producing strong easterly winds over the study site, peaking at over 25 m/s. A shorter-scale wind sea was generated in the open water region between Newfoundland and the ice pack, which propagated toward the north, into the ice pack, and was eventually attenuated by the ice cover. These waves arrived at the M/V *Terra Nordica* location with a 100-m wavelength, propagated toward the north, and had a significant wave height of about 0.4 m. This "wind sea" was present only on March 26.

Ice conditions during the experiment consisted of rafted, thin ice floes with a median thickness of 0.7 m and 100% ice coverage in the regions in which the IMPs were deployed. The individual ice floes were as large as 20 m in diameter, with a mean floe diameter of roughly 10 m. On March 26, the ice floes were tightly packed in a matrix of brash ice. Levees had built up around the ice floe edges due to wave-induced motion of the floes and the brash ice.

3.2. *Airborne SAR Measurements*

3.2.1. *SAR instrument summary.* Technical details concerning the SAR system flown on the CCRS CV-580 aircraft are given by *Livingstone et al.* [1988]. The C-band radar incorporates a dual-channel receiver and dual-polarized antenna; a seven-look, real-time SAR processor; range-dependent gain control (STC); and a real-time platform motion compensation system. The system is able to map to either side of the aircraft. Range compression is performed by surface acoustic wave (SAW) devices prior to digitization. Azimuth compression is usually carried out with the real-time SAR processor, providing the principal data source from the system. CCTs containing SAR imagery are subsequently produced on a transcription system located at CCRS in Ottawa. Postflight azimuth compression is possible, since the SAR signal data records are also recorded. For the LIMEX'89 data we were interested in individual look data, which required additional signal data processing. This processing was carried out at CCRS using a software-based SAR processor [*Raney and Vachon*, 1989].

3.2.2. *SAR data collection.* The CCRS SAR flight over the M/V *Terra Nordica* on March 26, 1989, is summarized in Table 1. A sample SAR image is shown in Figure 3. The SAR was configured to image ocean waves with various geometries with respect to the wave field. The platform height-to-velocity ratio (h/V) and the heading of the aircraft with respect to the waves was changed for successive passes.

3.2.3. *SAR data analysis.* Key parameters for the SAR geometry and processing for each line flown are shown in

TABLE 1. Summary of SAR and Spectral Parameters for March 26, 1992

Line/ Pass	Time, UTC	h, m	V, m/s	Track, deg	Look Direction	ϑ, deg	R, m	R/V, s	Δt, s
1/1	1734	3560	129	0	R	68	9,312	72	0.31
1/2	1801	3605	128	180	L	65	8,605	67	0.29
1/3	1825	6535	128	0	R	53	10,811	84	0.37
1/4	1853	6523	128	180	L	57	11,902	93	0.41

All data were acquired with VV polarization and processed to eight individual looks each separated in time by Δt. The scenes are located near the M/V *Terra Nordica* location. Also included are the look direction, which is right (R) or left (L), and the aircraft track with respect to North.

Table 1. Note, in particular, the time steps between successive looks. The SAR signal data were motion compensated and processed to eight individual looks. These looks were summed and examined for purposes of scene selection for spectral analysis. The corresponding individual look data were then subjected to SPS Fourier analysis [*Vachon and West*, 1992], compensated for the system transfer function [*Beal et al.*, 1983], speckle bias [*Goldfinger*, 1982], and scanning distortion [*Vachon et al.*, 1988], were smoothed, and had negative values set to zero. The resulting SAR image spectra have optimized contrast for the rather long SAR integration times, and for many cases, the ambiguity in propagation direction is resolved.

3.3. *IMP Observations*

3.3.1. *IMP instrument description.* On the basis of experience with measurements of iceberg motion and the LIMEX'87 measurements of wave-induced ice floe motion, C-CORE (St. John's, Newfoundland) designed a self-contained IMP [*McKenna and Crocker*, 1992], capable of measuring motion with 6 degrees of freedom: surge, heave, and sway (translational motions); pitch, roll, and yaw (rotational motions). This is accomplished by five sensors (three accelerometers, a vertical gyro, and a compass) housed in a sealed container along with associated electronics, data logger, and storage modules. A photograph of an IMP deployment is shown in Figure 4. The power is supplied by batteries housed in the box at the base of the container. The package was programmed to collect data in an intermittent mode at given intervals (usually for 30 min every hour).

The analogue signals from the sensors were passed through a 0.5-Hz antialiasing filter and were sampled at a rate of 4 Hz, which was subsequently reduced to 1.33 Hz using a digital filter on all but the compass record. The lower recording rate was needed in order to allow use of solid state storage devices.

3.3.2. *IMP data collection.* Deployments of IMPs were carried out by helicopter from M/V *Terra Nordica*. Generally, three or four packages were deployed at a time, though not all data were successfully recovered. Each IMP was placed upon an ice floe which was large enough to allow safe helicopter operations. Each IMP was accompanied by a set of corner reflectors which allowed identification of the location in the SAR imagery. Some of the instrumented ice floes also included a meteorological sampling package. Diagrams showing the relative locations of the SAR image data and the IMP deployments on March 26 are shown in Figure 5.

3.3.3. *IMP data analysis.* For the present study the data from the IMPs were treated as for a conventional heave/pitch/roll buoy, using the standard approach of Longuet-Higgins [see *Cartwright*, 1963; *Longuet-Higgins et al.*, 1963]. *Wadhams et al.* [1986] has previously used this technique for measuring wave decay in the MIZ. Using in situ instrumentation for measurement of wave spectra in ice-covered waters should be treated cautiously. Density and thickness anomalies, even in circular-shaped floes, can offset the centres of gravity and buoyancy, inducing cross-coupling effects between the rotational and translational motions. Larger ice floes also have a flexural response which is coupled to their rigid body motion, which modifies the dispersion relation. These effects are generally too complicated to address analytically. Numerical simulations of ice floes in waves [*Squire*, 1981] have shown, however, that when the floe diameter is less than or equal to one half the wavelength, the water-to-ice motion transfer function is close to unity.

For the IMP data, the five directional Fourier coefficients were estimated, as a function of frequency, using Longuet-Higgins' method. Full directional spectral estimates were obtained by using a maximum entropy directional analysis [*Lygre and Krogstad*, 1986]. The data were processed to give 16 degrees-of-freedom spectra using 1539 s of data with a frequency resolution of 0.0052 Hz in the 0.0052 to 0.66 Hz band. Directional slope spectra from the IMPs are included in Figure 5 and are discussed further and compared with SAR spectra in section 4.

4. ANALYSIS RESULTS

We now consider three separate case studies to better illustrate the proposed concepts of coherence time in SAR imaging and the role of the various velocity bunching FMMs. In the parametric study, we fit a quasi-linear FMM to the results of a nonlinear FMM in order to deduce the scale of τ_d. We then compare spectra from nearby regions showing waves-in-ice and open water in order to deduce the scale of τ_i. Finally, we apply the nonlinear FMM to measured IMP spectra for direct comparison with the observed SPS SAR image spectra.

4.1. *Parametric Study: Estimation of τ_d*

We carried out a parametric study to investigate the nonlinear effect of velocity bunching. The platform height parameter h was varied, while other parameters were held constant (V = 129 m/s, ϑ = 45°). The linear and nonlinear FMMs were applied to the IMP directional wave spectrum acquired by package 6 on March 26, 1989, at 1800 UTC. The simulations were designed such that the short north bound wave system was azimuth traveling. The input slope spec-

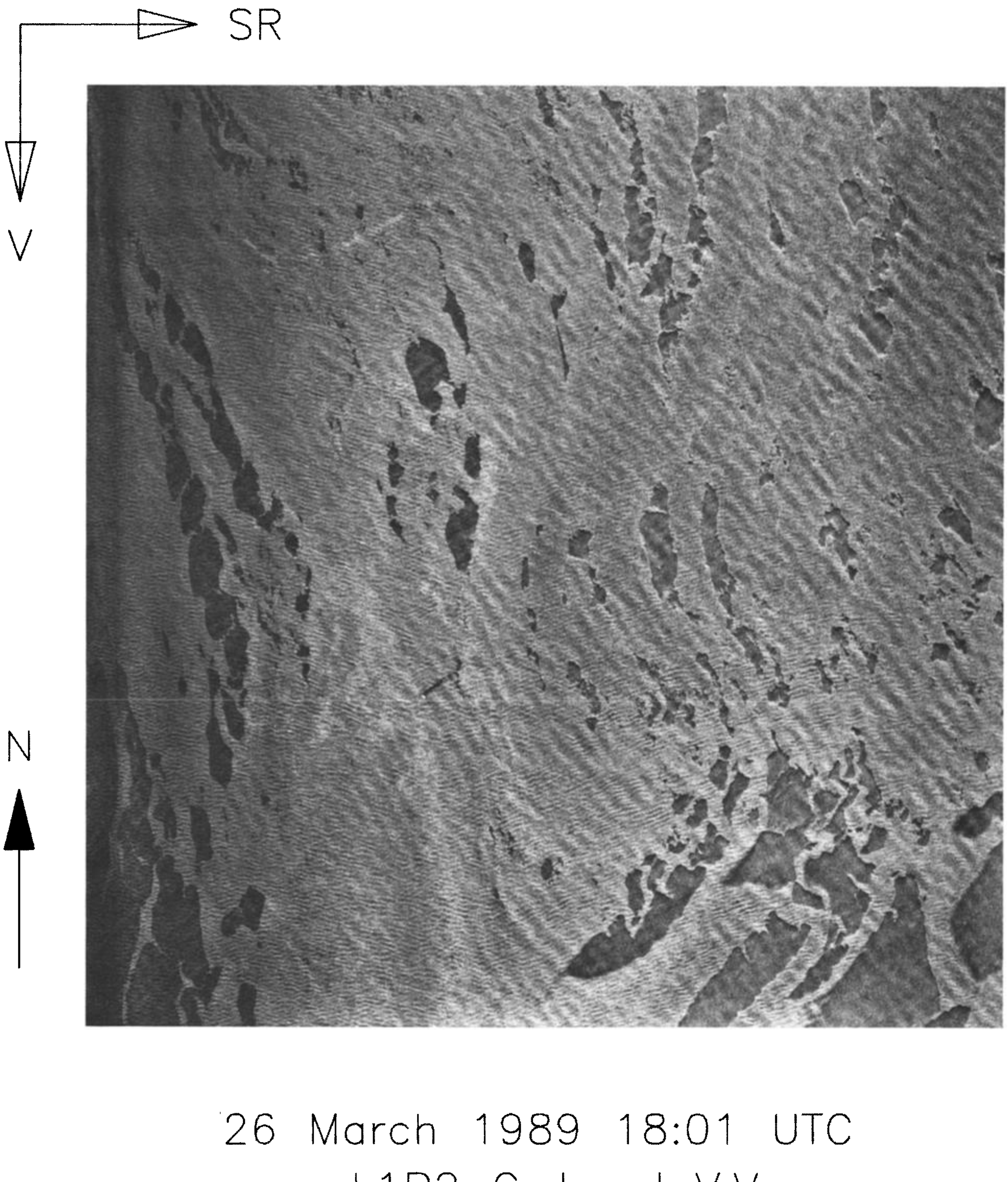

Fig. 3. An example CV-580 C-band SAR image acquired on March 26, 1989, during the LIMEX'89 field program. M/V *Terra Nordica* is located to the lower left of the image center. The image scale is 16 by 16 km in slant range (SR) and in azimuth (V).

trum and examples of the linear and nonlinear FMM results for various values of σ_ξ are shown in Figure 6.

In Figure 7, we have plotted the wave component amplitude for the wind sea and swell spectral components subject to the three velocity bunching FMMs and as a function of the nondimensional azimuth wavenumber κ. The cutoff wavelength for the quasi-linear model has been tuned to fit the nonlinear model based upon the measured spectral amplitude curves. The best fit cutoff wavelength for the quasi-linear model was found to be

$$\Lambda_c = 6.67\sigma_\xi, \tag{37}$$

which is the case presented in Figure 7. Excellent agreement between the quasi-linear and nonlinear FMMs may be imposed by restricting the domain of the fit (to a narrow range in σ_ξ or κ, for example). Now, using (26) and (37), we can

Fig. 4. Photograph showing a C-CORE IMP being deployed on an ice floe during LIMEX'89. The array of corner reflectors allowed identification of the IMP location in the SAR imagery.

rewrite the azimuth cutoff function which is due to the decorrelation time alone as

$$H_d(\bar{K}_k) = \exp\{-0.88\sigma_\xi^2\bar{K}_k^2\} \tag{38}$$

which is seen to roll-off more slowly than quasi-linear FMMs which are used elsewhere [*Hasselmann and Hasselmann*, 1991] for which the factor 0.88 is changed to unity.

Using (27), the corresponding decorrelation time scale for the input wave spectrum is then estimated to be

$$\tau_d = 415 \text{ [ms]}. \tag{39}$$

This value for τ_d applies only to this particular wave spectrum and the geometry of data acquisition (in terms of incidence angle and flight direction).

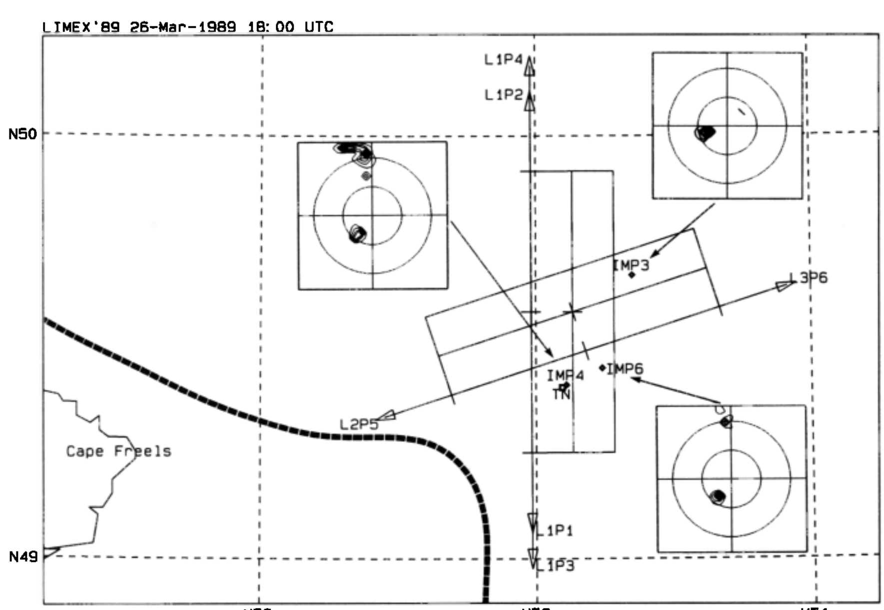

Fig. 5. Diagram showing the relative locations of the SAR data and IMP deployments on 26 March 1989. The line (L) and pass (P) numbers for the SAR data are indicated near the start of each flight line. The M/V *Terra Nordica* location is indicated by TN. Representative directional slope spectra (going-to convention) for the IMPs at 1800 UTC are also shown. For the spectra the outer circle represents 100-m wavelengths and the inner circle 200 m wave lengths. The heavy dashed line indicates the nominal southern extent of dense ice cover.

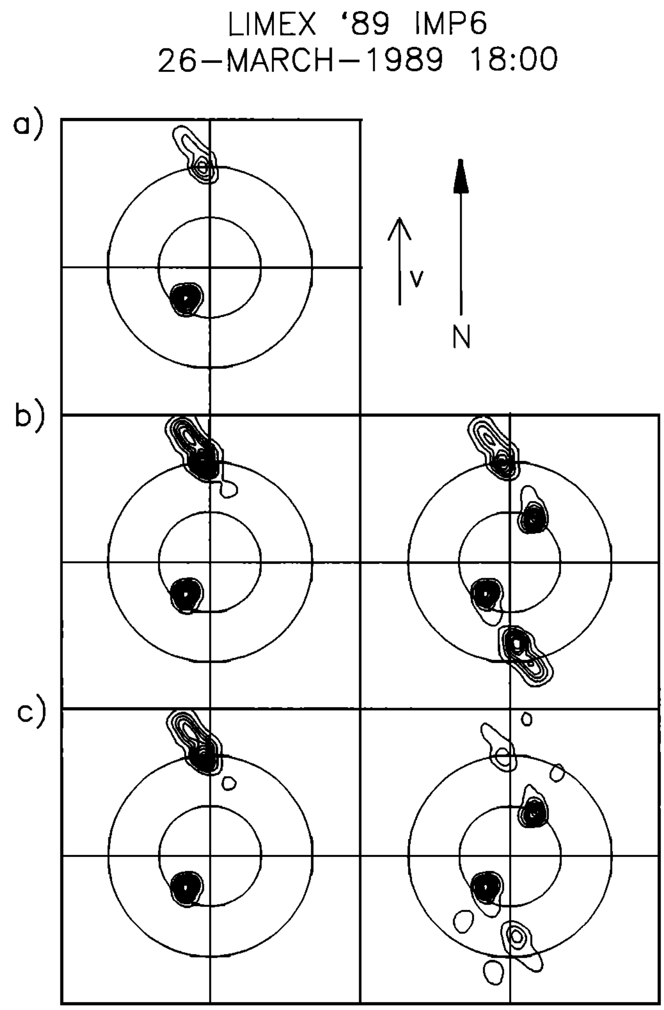

Fig. 6. Velocity bunching parametric study results: (*a*) the input IMP 6 directional slope spectrum; (*b*) forward mapped SAR image spectra for the linear (left) and the nonlinear (right) models for σ_ξ = 4 m; and (*c*) forward mapped SAR image spectra for σ_ξ = 20 m. In each case, north is up, the outer circle represents 100-m wavelengths, and the inner circle represents 200-m wavelengths. The correctly propagating peak directions (going to) are indicated by the spectrum in Figure 6*a*.

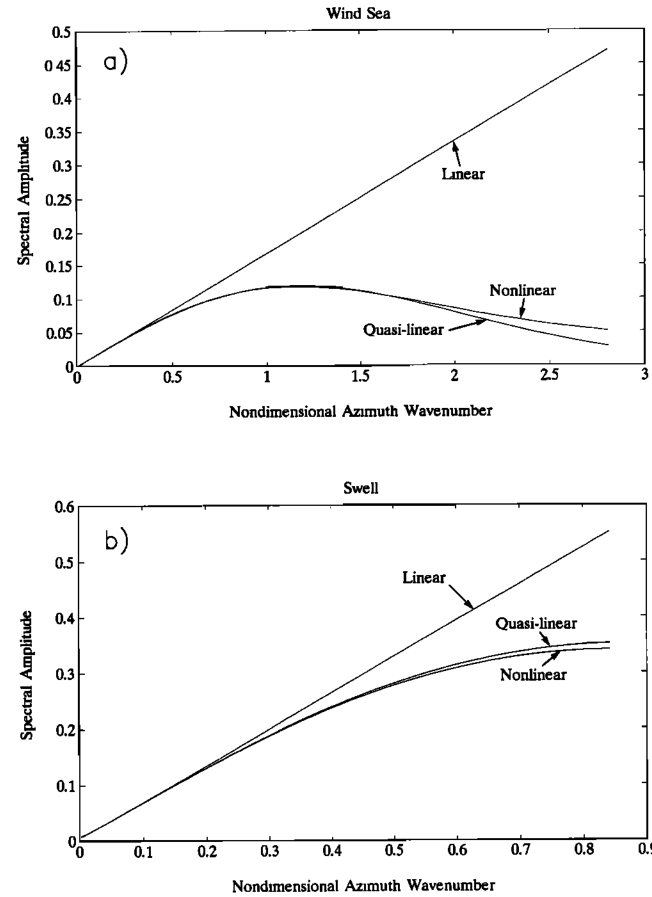

Fig. 7. Plots of (*a*) wind sea and (*b*) swell amplitude from the parametric study for linear, tuned quasi-linear, and nonlinear FMMs as a function of κ.

Other parameterizations for Λ_c are possible, such as proportionality to the square root of the significant wave height. However, the chosen form, and any other based upon wave properties only, includes only the effects of velocity bunching. No intrinsic scatterer behavior has been included in this parametric study.

From Figures 6 and 7 we see the following:

1. The input IMP spectrum considered in this parametric study has very narrow spectral peaks (in direction and wavenumber). For such cases, as illustrated by Figure 6*c*, higher order harmonics have appeared in the simulated SAR image spectrum when using the fully nonlinear FMM. For this case, the crests would appear to be cusplike in the SAR image. Neither the linear nor the quasi-linear FMMs could predict this effect.

2. Although not physically realizable, only the smallest values of h/V, hence σ_ξ and κ, show any effects of tilt modulation, and then only for the swell which has a range traveling wavenumber component (note in Figure 7*b* that the spectral amplitude does not go to zero for $\sigma_\xi \rightarrow 0$).

3. For both the swell and wind sea, there is a small region over which the amplitude changes in proportion to σ_ξ, such that the linear FMM applies. For a maximum of 10% error in spectral amplitude, we define the region of applicability for the linear model to be $\kappa < 0.3$ for both the wind sea and the swell.

4. For both the swell and wind sea there is a larger region over which the tuned quasi-linear FMM applies. For a maximum of 10% error in amplitude, we define the region of applicability for the quasi-linear model to be $\kappa < 2.1$ for the observed wind sea; however, the 10% error limit for swell was not approached for the range in κ considered.

In this parametric study, we have tuned a quasi-linear FMM to fit the azimuth cutoff wavelength predicted by the nonlinear FMM, for modest values of κ. The quasi-linear FMM cutoff wavelength could be tuned to the nonlinear FMM such that it would apply to larger values of κ but then, only over a rather limited range for this parameter. Derivation of an analytic form which matches a quasi-linear FMM to the expected cutoff wavelength of the nonlinear FMM is the subject of ongoing research.

4.2. *Ice Versus Open Water: Estimation of τ_i*

We now compare the azimuth cutoff wavelength for waves in ice and open water. For this comparison, we will use the ratio technique of *Johnsen et al.* [1991] which they have successfully used to estimate relative spectral widths and

TABLE 2. Summary of Estimated Intrinsic Coherence Time Scales From the Ice-Covered and Open Water Comparison

Line/ Pass	R, m	R/V, s	K_{ci}, rad/m	σK_{ci}, rad/m	τ_i, ms
1/1	7340	57	0.143	0.065	163
1/2	6603	52	0.148	0.081	153
1/3	9225	72	0.097	0.017	140
1/4	9311	73	0.112	0.022	162
Average					154 ± 30

azimuth cutoff length scales. In the case of waves in ice versus open water, we assume that the input ocean spectrum, the linear portions of the modulation transfer function, and the azimuth cutoff due to scatterer decorrelation τ_d are equivalent for the two cases. The main difference in the spectra, therefore, must arise from the intrinsic scatterer behavior for the open water case τ_i. Then, the ratio of the open water SAR image spectrum $S_o(K_k, K_l)$ to the ice covered SAR image spectrum $S_i(K_k, K_l)$ is

$$\frac{S_o(K_k, K_l)}{S_i(K_k, K_l)} = \exp\left\{-\pi\left(\frac{\tilde{K}_k}{K_{ci}}\right)^2\right\}, \qquad (40)$$

where K_{ci} is the cutoff wavenumber due to the intrinsic scene coherence time for open water. The intrinsic scene coherence time then may be calculated in accordance with (27).

Ratios between spectral wavenumber bins were computed for pairs of ice and open water spectra obtained from different ranges for each pass. In this case, imagery from the CCRS SAR's real-time processor was used. This presents no complication since contrast degradation due to look misregistration will be equivalent for pairs of spectra derived from the same range. Equation (40) was solved for K_{ci} for each wavenumber bin which contained wave spectral energy. This approach allowed determination of an average K_{ci} and its standard deviation for each pair of ice and open water spectra.

The results are given in Table 2, and an example of ice and open water spectra and their best fit based upon (40) are shown in Figure 8. For the four cases which allow independent estimation of τ_i we find that

$$\tau_i = 154 \pm 30[\text{ms}]. \qquad (41)$$

This intrinsic coherence time applies to the LIMEX'89 open ocean observations which were taken with a wind speed of 12 m/s. For the general open ocean case, τ_i would scale from this measured value, perhaps depending upon wind speed.

A complete quasi-linear FMM should include the velocity bunching decorrelation time scale found in section 4.1, and the intrinsic coherence time scale found here, combined in accordance with equation (1). We see that for the open water cases observed during LIMEX'89, the coherence time was dominated by the intrinsic coherence time scale ($\tau_i \sim 154$ ms), which was significantly shorter than the decorrelation time scale ($\tau_d \sim 415$ ms). Using (27) and the measured coherence times, the cutoff wave length for waves in ice was $\Lambda_c \sim 0.59(R/V)$ and for open water was $\Lambda_c \sim 2.1(R/V)$. The significant difference in the cutoff length scale is readily apparent from inspection of the image of Figure 3 for which the wind sea is visible in the ice-covered regions, but not in the open water regions, especially at far range (when (R/V) is largest).

It is also worthwhile to determine if the SAR was actually operating in a scene coherence time limited mode, for either the waves-in-ice or open water cases. Using (24) and the processed beam width of 1.75°, the SAR is coherence time limited by τ_i if $(R/V) > 4$ s and is coherence time limited by τ_d if $(R/V) > 12$ s. Therefore the airborne SAR was coherence time limited for all of the data sets we examined in this study.

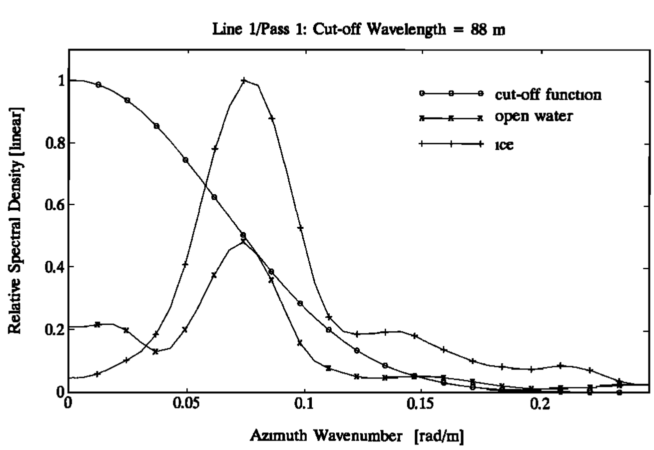

Fig. 8. Comparison of azimuth SAR image spectra from ice-covered and nearby open water regions and the quasi-linear azimuth cutoff function which best relates the two. The aircraft and wind sea of interest were both north-bound.

4.3. *FMM Results*

Spectral comparisons between corrected SAR SPS spectra from March 26, 1989, and the nonlinear FMM applied to nearby IMP spectra collected at 1800 UTC on the same date, are shown in Figure 9. The SPS processing changes the relative energy distribution in the wind sea and swell peaks in the SAR spectra and has largely resolved the wave propagation direction (on the basis of the largest peak of the formerly completely ambiguous pair). The change in relative energy is a result of the procedure compensating for wave translation between successive looks.

In order to assess our ability to predict the observed SAR spectra from the measured IMP spectra, quantitative measures of the individual wind sea and swell spectral peaks have been extracted from the spectral data sets. Table 3 shows peak values, directions, and wavelengths based upon integration over spectral values which are greater than 50% of the spectral peak of interest, in accordance with equations (6) and (7).

For the purpose of spectral comparison, the spectral peak values have been normalized to the wind sea peak for the case of line 1/pass 1. For the IMP spectra, package 6 was used as the reference. This normalization allows consistent comparison of peak values for all cases. Table 3 also includes σ_ξ based upon each IMP spectrum and the geometry of each pass, and the ratio of wind sea to swell spectral peak.

From Table 3, the following are apparent:

1. κ is small in nearly all cases suggesting that a linear MTF might be adequate for the wave spectra observed in LIMEX'89, especially for the swell.

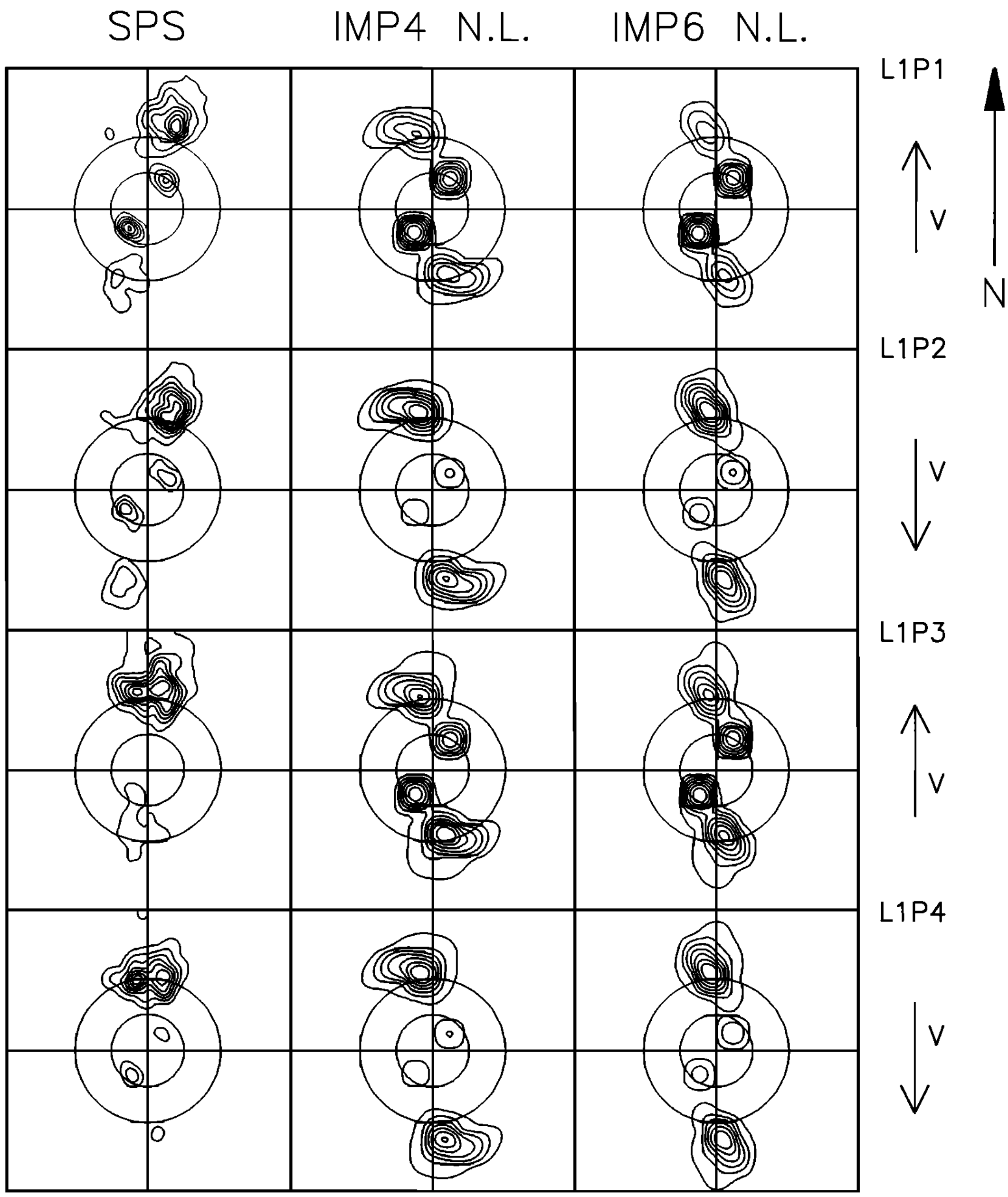

Fig. 9. Spectral-phase-shift (SPS) spectra for a SAR scene near M/V *Terra Nordica* and nonlinear (NL) forward mapped IMP spectra from packages 4 and 6. In each case, north is up, the outer circle represents 100-m wavelengths, and the inner 200-m wavelengths. The arrows indicate the platform flight direction for each line and pass. The correctly propagating peak directions are north bound for the wind sea and southwest bound for the swell.

2. A quasi-linear model is an excellent representation of the SAR MTF for all of the wave spectra and platform geometries considered, even for the case of the azimuth traveling wind sea.

3. The peak wavelength and direction for the wind sea peak and the swell are consistently measured between the SAR SPS spectra and the forward mapped IMP spectra.

4. The ratio of sea to swell spectral peaks is a sensitive measure of the success in applying a FMM to an IMP spectrum. From Table 3 the spectral peak ratio in the IMP heave spectra is about -10 dB, while for the forward mapped spectra this ratio is as large as $+10$ dB. Also, the peak ratios for the forward mapped IMP spectra are consistent with those observed in the SPS spectra to within 6 dB, except for the case of line 1/pass 3.

Although the rather poor results of the line 1/pass 3 IMP forward mapping results in terms of the wind sea to swell peak ratio is not understood, it is rather satisfying that three of the four cases considered resulted in reasonable agreement (within a factor of 4 for the wind sea to swell peak ratio). This reasonable agreement between IMP forward mapping results and observed SAR SPS spectra requires that five separate conditions or requirements be simultaneously and adequately satisfied.

The first requirement is that there be a small spatial separation between the SAR observations and IMP measure-

TABLE 3. Summary of Spectral Peak Analysis Results for the Wind Sea and Swell Observed on March 26, 1992

			Sea				Swell				
	Line/Pass	σ_ξ, m	S_{sea}	Λ_0, m	φ, deg	κ	S_{swell}	Λ_0, m	φ, deg	κ	S_{sea}/S_{swell}, dB
SAR	1/1		1.0	81	17		0.3	268	219		5.1
IMP 4		5.9	1.6	89	345	0.40	1.3	247	216	0.12	0.9
IMP 6		5.3	1.0	93	353	0.36	1.2	254	218	0.10	−0.8
SAR	1/2		2.1	86	16		0.3	245	224		8.3
IMP 4		5.6	2.4	86	346	0.40	0.3	258	219	0.11	9.3
IMP 6		5.0	1.5	89	354	0.35	0.3	254	218	0.10	6.7
SAR	1/3		7.7	88	4		0.5	252	206		11.9
IMP 4		7.9	3.5	92	348	0.53	2.0	243	216	0.17	2.5
IMP 6		7.2	2.6	95	354	0.47	2.1	252	217	0.14	1.0
SAR	1/4		7.0	98	3		0.7	247	214		10.2
IMP 4		8.3	4.8	89	349	0.58	0.7	260	218	0.16	8.3
IMP 6		7.5	3.3	93	355	0.50	0.7	253	217	0.15	6.5
IMP 4	heave		1.5	97	353		11.9	279	219		−9.1
IMP 6	heave		1.0	102	356		9.1	277	216		−9.6

S_{sea} and S_{swell} are the peak values for the wind sea and swell spectral peaks, respectively, and φ is the propagation direction with respect to North.

ments. The ice cover causes rapid changes in the wave spectral density as a function of spatial position due to wave attenuation (especially for the wind sea). This is evident by inspection of Figure 5 which shows that the IMP spectrum from package 3, which was the north-most location on March 26, showed no signature whatsoever of the wind sea. In the case of our comparisons, the SAR image spectrum was taken near M/V *Terra Nordica*, which was close to the location of package 4. Package 6, which was also included in the comparison, was less than 10 km away.

The second requirement is that there be a small temporal separation between the observations. Note that for these cases, the IMP recordings started at 1800 UTC and went on for 1539 s. On the other hand, the SAR spectra were obtained between about 1730 and 1900 UTC (see Table 1). The temporal agreement between all spectral sources is rather good.

The third requirement is that the dispersion relation be well known. This is explicitly required since SAR spatial measurements are being compared with heave/pitch/roll time series measurements. It is well known that an ice cover will modify the dispersion relation for some length scales [*Liu and Mollo-Christensen*, 1988; *Liu et al.*, 1991*a*]. However, in this work, an open water dispersion relation was used since the ice cover was rather thin, and the wave scales of interest were rather long compared to the scale of the ice floes which were present.

The fourth requirement is that the SPS spectral analysis of the SAR data be successful. If SPS spectral analysis is not used, our experiments have shown that the ratio of wind sea to swell spectral peak ratio will be underestimated by up to 5 dB. This is due to the SAR peak spectral density being degraded differentially as a function of wavenumber. For this analysis, we chose eight looks, each separated by time steps Δt indicated in Table 1. Selection of a different number of looks or time step between successive looks would affect the wind sea to swell spectral peak ratio.

The fifth requirement is that the spectral analysis techniques used to derive directional spectra from the IMP measurements actually apply to the case of waves in ice. We used standard techniques developed for floating wave buoys. These techniques should be good approximations provided that the ice floes are small in diameter compared to the length of the waves themselves. This requirement is complicated by the presence of crossing wave systems in our data sets. Furthermore, the rather small spectral certainty for the IMP spectra (16 degrees of freedom) results in a rather large confidence intervals for the IMP spectra, the standard deviation of each estimated spectral density being about 35%.

5. CONCLUSIONS

In this paper we have considered results from the spectral analysis of SAR imagery of waves in ice collected during LIMEX'89. The appearance of the spectra is supported by known theoretical considerations, including velocity bunching mapping, scene coherence time limitations, tilt modulation, and wave evolution in the marginal ice zone.

One of our main objectives was to study and establish the time scales for coherence time limited imaging by a SAR of ocean surface waves. We considered a model in which the effective coherence was comprised of two separable parts. First, the decorrelation time scale τ_d arises directly from velocity bunching and Bragg scattering patches moving with respect to one another. Second, the intrinsic coherence time scale τ_i arises from the Bragg scattering patches actually changing over time.

The LIMEX'89 observations are of interest in understanding these two coherence time scales since these time scales apply differently to waves in ice and waves in open water. For both cases, the effects of τ_d should apply in an equivalent manner, assuming that the wave spectrum is unchanged by the presence of an ice cover. On the other hand, the effect of τ_d should apply only to the case of open water waves since the scattering from the ice covered case should be time invariant. The Bragg-scale patches in open water are subject to deformation and change over short time scales given by τ_i, due to wind forcing and wave-wave interactions.

In this paper we have made independent estimates of these two coherence time scales. Each estimate was based upon using a quasi-linear velocity bunching model, in which an azimuth cutoff function was introduced to describe the reduction in azimuth resolution for coherence time limited SAR imaging. The decorrelation time scale was estimated by fitting the quasi-linear velocity bunching model to the predictions of the nonlinear velocity bunching model. The intrinsic scene coherence time was estimated by comparing SAR image spectra derived from nearby waves in ice and open water cases.

The decorrelation time scale was estimated to be $\tau_d \sim 415$ ms for the rather placid conditions during the field program (for 1-m significant wave height, wind sea, and swell systems present) while the intrinsic scene coherence time was estimated to be $\tau_i \sim 154$ ms (for 12 m/s wind speed). Thus, for the LIMEX'89 spectra considered in this paper, the coherence time for the open water case is dominated by the intrinsic coherence time scale.

The intrinsic coherence time is likely strongly dependent upon wind speed. A possible scaling for τ_i is with the inverse of wind speed or wind stress.

It is clear that the effect of τ_i on azimuth resolution is an essential part of the ocean wave to SAR image forward mapping problem. Consequently, when inverting SAR image spectra to ocean wave spectra, an iterative process [*Hasselmann and Hasselmann*, 1991] which depends upon the physics in the FMM being correct, the intrinsic scene coherence time scale should also be included. We believe that this is particularly true if the wind speed is high (say, greater than 10 m/s). Otherwise, the degree of azimuth cutoff in the FMM will be underestimated (the effective coherence time will be smaller than that predicted by τ_d alone). The present inversion algorithms would adaptively try to correct for this effect by forcing τ_d to become smaller. This could translate into an overestimate in wave height, for example, in the inverted SAR spectrum.

It was shown that for the case of waves in ice a quasi-linear velocity bunching FMM provides reasonable agreement between observed IMP spectra and SPS processed airborne SAR image spectra. Although the wave conditions considered were rather placid, the ratio R/V was as large as 93 s. The ratio of wind sea to swell spectral peak was shown to be -10 dB for the observed IMP heave spectra, but as large as $+10$ dB for the forward mapped spectra. Three of the four cases considered showed good agreement (within a factor of 4) in terms of the wind sea to swell spectral peak ratio.

Following this work, several issues still remain to be resolved in SAR imaging of ocean waves. In particular, the scaling of τ_i with wind and wave conditions is an essential requirement. Unfortunately, the LIMEX'89 observations only provide us with data from a single wind speed and sea state condition. Further tuning of the quasi-linear model in order to deduce the scaling of τ_i is possible. Spacecraft and airborne SAR data sets acquired under a variety of wind and wave conditions and with adequate in situ validation information will be helpful in further defining τ_i. This is the subject of ongoing research based upon simultaneously acquired ERS-1 and CV-580 SAR data sets [see *Dobson et al.*, 1993].

Acknowledgments. The authors wish to thank their families for their support and encouragement. We also wish to thank the LIMEX'89 experimental team, in particular the crews of M/V *Terra Nordica* and the CCRS CV-580, for their efforts in the successful collection of these data. C-CORE developed the IMPs and supplied the ice motion time series. The SAR data were processed to individual looks by J. Wolfe (Intera Kenting). Various portions of the spectral processing were carried out at CCRS by S. Paterson (Intera Kenting), A. S. Bhogal (Intera Kenting), S. Bottoms, and J. Martin. The figures were drafted by R. Staples (CCRS). We thank R. K. Raney (CCRS) for helpful discussion and comments on the manuscript.

REFERENCES

Alpers, W. R., Monte Carlo simulations for studying the relationship between ocean wave and synthetic aperture radar image spectra, *J. Geophys. Res.*, *88*(C3), 1745–1759, 1983.

Alpers, W. R., and C. L. Rufenach, The effect of orbital motions on synthetic aperture radar imagery of ocean waves, *IEEE Trans. Antennas Propagat.*, *AP-27*(5), 685–690, 1979.

Alpers, W. R., D. B. Ross, and C. L. Rufenach, On the detectability of ocean surface waves by real and synthetic aperture radar, *J. Geophys. Res.*, *86*(C7), 6481–6498, 1981.

Beal, R. C., D. G. Tilley, and F. M. Monaldo, Large- and small-scale spatial evolution of digitally processed ocean wave spectra from Seasat synthetic aperture radar, *J. Geophys. Res.*, *88*(C3), 1761–1778, 1983.

Borgman, L. E., Directional spectra from wave sensors, in *Ocean Wave Climate*, *Mar. Sci. Ser.*, vol. 88, pp. 269–300, Plenum, New York, 1979.

Cartwright, D. E., The use of directional spectra in studying the output of a wave recorder on a moving ship, in *Ocean Wave Spectra*, pp. 203–218, Prentice-Hall, Englewood Cliffs, N. J., 1963.

Dobson, F. W., S. D. Smith, R. J. Anderson, P. W. Vachon, D. Vandemark, J. R. Buckley, M. Allingham, M. Khandekar, R. Lalbeharry, and E. Gill, The Grand Banks ERS-1 SAR wave experiment, *Eos Trans. AGU*, *74*(4), 41, 44–45, 1993.

Goldfinger, A., Estimation of spectra from speckled images, *IEEE Trans. Aerosp. Electron. Syst.*, *AES-18*(5), 675–681, 1982.

Hasselmann, K., and S. Hasselmann, On the nonlinear mapping of an ocean wave spectrum into a SAR image spectrum and its inversion, *J. Geophys. Res.*, *96*(C6), 10,713–10,729, 1991.

Hasselmann, K., R. K. Raney, W. J. Plant, W. Alpers, R. A. Shuchman, D. R. Lyzenga, C. L. Rufenach, and M. J. Tucker, Theory of synthetic aperture radar ocean imaging: A MARSEN view, *J. Geophys. Res.*, *90*(C3), 4659–4686, 1985.

Johnsen, H., K. A. Høgda, T. Guneriussen, and J. P. Pedersen, Azimuth smearing in synthetic aperture radar ocean image spectra from the Norwegian Continental Shelf Experiment of 1988, *J. Geophys. Res.*, *96*(C6), 10,443–10,453, 1991.

Kawai, S., Generation of initial wavelets by instability of a coupled shear flow and their evolution to wind waves, *J. Fluid Mech.*, *93*, 661–703, 1979.

Krogstad, H. E., A simple derivation of Hasselmann's nonlinear ocean-SAR transform, *J. Geophys. Res.*, *97*(C2), 2421–2425, 1992.

Liu, A. K., and E. Mollo-Christensen, Wave propagation in a solid ice pack, *J. Phys. Oceanogr.*, *18*(11), 1702–1712, 1988.

Liu, A. K., B. Holt, and P. W. Vachon, Wave propagation in the marginal ice zone: Model predictions and comparisons with buoy and synthetic aperture radar data, *J. Geophys. Res.*, *96*(C3), 4605–4621, 1991*a*.

Liu, A. K., P. W. Vachon, and C. Y. Peng, Observation of wave refraction at an ice edge by synthetic aperture radar, *J. Geophys. Res.*, *96*(C3), 4803–4808, 1991*b*.

Liu, A. K., P. W. Vachon, C. Y. Peng, and A. S. Bhogal, Wave attenuation in the marginal ice zone during LIMEX, *Atmos. Ocean*, *30*(2), 192–206, 1992.

Livingstone, C. E., A. L. Gray, R. K. Hawkins, and R. B. Olsen, CCRS C/X-airborne synthetic aperture radar: An R and D tool for the ERS-1 time frame, *IEEE AES Mag.*, *3*(10), 11–20, 1988.

Longuet-Higgins, M. S., D. E. Cartwright, and N. D. Smith, Observations of the directional spectrum of sea waves using the motions of a floating buoy, in *Ocean Wave Spectra*, pp. 111–136, Prentice-Hall, Englewood Cliffs, N. J., 1963.

Lygre, A., and H. E. Krogstad, Maximum entropy estimation of the directional distribution of ocean wave spectra, *J. Phys. Oceanogr.*, *16*(12), 2052–2060, 1986.

McKenna, R. F., and G. B. Crocker, Ice-floe collisions interpreted from acceleration data during LIMEX'89, *Atmos. Ocean.*, *30*(2), 246–269, 1992.

Monaldo, F. M., and D. R. Lyzenga, On the estimation of wave-slope and wave height variance spectra from SAR imagery, *IEEE Trans. Geosci. Remote Sens.*, *GE-24*(4), 543–551, 1986.

Parzen, E., *Stochastic Processes*, Holden-Day, Oakland, Calif., 1962.

Raney, R. K., Synthetic aperture imaging radar and moving targets, *IEEE Trans. Aerosp. Electron. Syst.*, *AES-7*(3), 499–505, 1971.

Raney, R. K., SAR response to partially coherent phenomena, *IEEE J. Trans. Antenna Propagat.*, *AP-26*(6), 777–787, 1980.

Raney, R. K., Wave orbital velocity, fade, and SAR response to azimuth waves, *IEEE J. Oceanic Eng.*, *OE-6*(4), 140–146, 1981.

Raney, R. K., and P. W. Vachon, A phase preserving SAR processor, in *Proceedings of IGARSS'89/12th Canadian Symposium on Remote Sensing*, pp. 2588–2591, Institute of Electrical and Electronics Engineers, New York, 1989.

Raney, R. K., P. W. Vachon, R. A. DeAbreu, and A. S. Bhogal, Airborne SAR observations of ocean surface waves penetrating floating ice, *IEEE Trans. Geosci. Remote Sens.*, *27*(5), 492–500, 1989.

Squire, V. A., Numerical simulation of ice floes in water, *Tech. Rep. 81-1*, Scott Polar Res. Inst., Cambridge, England, 1981.

Swift, C. T., and L. R. Wilson, Synthetic aperture radar imaging of moving ocean waves, *IEEE Trans. Antennas Propagat.*, *AP-27*(6), 725–729, 1979.

Tang, C. L., and M. Manore (Guest Eds.), LIMEX special issue, *Atmos. Ocean*, *30*(2), 147–296, 1992.

Tucker, M. J., The imaging of waves by satelliteborne synthetic aperture radar: The effects of sea-surface motion, *Int. J. Remote Sens.*, *6*(7), 1059–1074, 1985.

Vachon, P. W., Synthetic-aperture radar imaging of the ocean surface: Theoretical considerations, and experiments with simulated and actual SAR imagery, Ph.D. thesis, Dep. of Oceanogr., Univ. of B. C., Vancouver, 1987.

Vachon, P. W., and A. S. Bhogal, Airborne SAR observations of ocean waves during LIMEX 1989, in *Proceedings of 13th Canadian Symposium on Remote Sensing*, pp. 460–469, Department of Surveying Engineering, University of New Brunswick, Fredericton, 1990.

Vachon, P. W., and R. K. Raney, Resolution of the ocean wave propagation direction in SAR imagery, *IEEE Trans. Geosci. Remote Sens.*, *29*(1), 105–112, 1991.

Vachon, P. W., and R. K. Raney, Ocean waves and optimal SAR processing: Don't adjust the focus!, *IEEE Trans. Geosci. Remote Sens.*, *30*(3), 627–630, 1992.

Vachon, P. W., and J. C. West, Spectral estimation techniques for multilook SAR images of ocean waves, *IEEE Trans. Geosci. Remote Sens.*, *30*(3), 568–577, 1992.

Vachon, P. W., R. B. Olsen, C. E. Livingstone, and N. G. Freeman, Airborne SAR imagery of ocean surface waves obtained during LEWEX: Some initial results, *IEEE Trans. Geosci. Remote Sens.*, *26*(5), 548–561, 1988.

Wadhams, P., V. A. Squire, J. A. Ewing, and R. W. Pascal, The effect of the marginal ice zone on the directional wave spectrum of the ocean, *J. Phys. Oceanogr.*, *16*, 358–376, 1986.

Wright, J. W., Backscattering from capillary waves with application to sea clutter, *IEEE Trans. Antennas Propagat.*, *AP-14*(6), 749–754, 1966.

H. E. Krogstad, SINTEF Industrial Mathematics, N-7034 Trondheim, Norway.

A. K. Liu, NASA Goddard Space Flight Center, Code 971, Greenbelt, MD 20771.

R. B. Olsen, Satlantic Inc., 3295 Barrington St., Halifax, N. S., Canada B3K 5X8.

P. W. Vachon, Canada Centre for Remote Sensing, 588 Booth St., Ottawa, Ont., Canada K1A 0Y7.

(Received January 4, 1993;
revised April 6, 1993;
accepted April 6, 1993.)